

<https://doi.org/10.1038/s43247-024-01329-3>

Radiative forcing geoengineering causes higher risk of wildfires and permafrost thawing over the Arctic regions

Check for updates

Rhonda C. Müller^{1,2}✉, Jin-Soo Kim^{3,4}✉, Hanna Lee^{5,6}, Helene Muri⁷, Jerry Tjiputra⁶, Jin-Ho Yoon⁸ & Gabriela Schaepman-Strub¹

Radiative forcing geoengineering is discussed as an intermediate solution to partially offset greenhouse gas-driven warming by altering the Earth's energy budget. Here we use an Earth System Model to analyse the response in Arctic temperatures to radiative geoengineering applied under the representative concentration pathway 8.5 to decrease the radiative forcing to that achieved under the representative concentration pathway 4.5. The three methods Stratospheric Aerosol Injection, Marine Cloud Brightening, and Cirrus Cloud Thinning, mitigate the global mean temperature rise, however, under our experimental designs, the projected Arctic temperatures are higher than if the same temperature was achieved under emission mitigation. The maximum temperature increase under Cirrus Cloud Thinning and Marine Cloud Brightening is linked to carbon dioxide plant physiological forcing, shifting the system into climatic conditions favouring the development of fires. Under Stratospheric Aerosol Injection, the Arctic land with temperatures permanently below freezing decreased by 7.8% compared to the representative concentration pathway 4.5. This study concludes that these specific radiative forcing geoengineering designs induce less efficient cooling of the Arctic than the global mean and worsen extreme conditions compared to the representative concentration pathway 4.5.

In 2015, 196 nations agreed to limit the global mean temperature increase to 2 °C—aiming for 1.5 °C—in the Paris Agreement treaty¹. For the first time, global nations united to take action against climate change, which is seen by many as a milestone in the attempts to limit temperature increase on a global scale. However, this requires all countries to accelerate their implementation of policies to reach the required reduction in anthropogenic carbon dioxide (CO₂) emissions. Current estimates factoring in national policies assume a median emission reduction gap by 2030 of approximately 22.4 GtCO₂-equivalent for the 2 °C pathway², when CO₂ emissions should have decreased by 45% compared to 2010³.

In the meantime, geoengineering is being discussed as an option to partially offset anthropogenic climate warming to buy time to reduce

greenhouse gas emissions and develop mitigation strategies. The most commonly discussed types of geoengineering are Carbon Dioxide Removal (CDR) and Radiative Forcing Geoengineering (RFG). While CDR aims to remove CO₂ from the atmosphere, for example by enhancing weathering or afforestation, RFG would alter the Earth's radiation budget^{4,5}. We have chosen the term RFG here, in contrast to e.g., Solar Radiation Management, as it is inclusive of methods that alter the longwave radiation budget of the Earth. Of these two, only CDR addresses the root of the problem by targeting a CO₂ reduction in the atmosphere. It would, however, take decades to implement efficient CDR methods on a large scale and require more resources than RFG in the process^{4,6,7}. RFG could be deployed within a few years, pending sufficient research and development, with an almost

¹Department of Evolutionary Biology and Environmental Studies, University of Zurich, Zurich, Switzerland. ²Department of Geography, University of Zurich, Zurich, Switzerland. ³Low-Carbon and Climate Impact Research Centre, School of Energy and Environment, City University of Hong Kong, Hong Kong, China. ⁴Center for Ocean Research in Hong Kong and Macao (CORE), The Hong Kong University of Science and Technology, Hong Kong, China. ⁵Department of Biology, Norwegian University of Science and Technology, Trondheim, Norway. ⁶NORCE Norwegian Research Institute, Bjerknes Centre for Climate Research, Bergen, Norway. ⁷Industrial Ecology Programme, Department of Energy and Process Engineering, Norwegian University of Science and Technology, Trondheim, Norway. ⁸School of Earth Sciences and Environmental Engineering, Gwangju Institute of Science and Technology, Gwangju, South Korea. ✉e-mail: rhonda.c.mueller@gmail.com; jinsoo.kim@cityu.edu.hk

immediate effect on the climate. It has been proposed that RFG could be useful to rapidly cool the climate, for example to keep the Earth system from reaching tipping points^{4,7}. While there are no clear cost estimates for Cirrus Cloud Thinning and Marine Cloud Brightening, Stratospheric Aerosol Injection was estimated to cost around \$18 billion year⁻¹ per degree Celsius of global warming avoided⁸.

Three RFG methods are commonly considered among scientists: Cirrus Cloud Thinning (CCT), Marine Cloud Brightening (MCB) and Stratospheric Aerosol Injection (SAI). CCT aims to increase the outgoing longwave radiation at the top of the atmosphere by thinning high cirrus clouds that trap longwave radiation within the Earth system⁹. MCB and SAI both act on the shortwave radiation budget of the climate system. Specifically, MCB aims to increase cloud albedo and reflection of sunlight over oceans^{10,11}, while SAI aims to build a layer of aerosols in the stratosphere that scatters part of the incoming solar radiation, increasing the Earth's planetary albedo¹². Without removing CO₂ from the atmosphere, all three RFG methods would require a long-term implementation to maintain global cooling. RFG termination would lead to a rapid increase in global temperature^{4,5}.

Earth System Models have been used to assess the impacts of large-scale RFG on various aspects of the Earth system to fully understand the feedbacks and consequences of RFG application. We use the Norwegian Earth System Model (NorESM1-ME)^{13,14} to understand the responses and feedbacks of terrestrial systems. We apply the three most commonly discussed RFG methods; (i) CCT by increasing the fall speed of ice crystals for temperatures below -38 °C, (ii) MCB by increasing the natural emission at the ocean surface of sea salt aerosols in the accumulation mode into the atmosphere between the latitudes of 45°S and 45°N, increasing the cloud albedo over land and ocean and (iii) SAI by prescribing the properties of an injected layer of sulphur dioxide in the stratosphere in a grid cell close to the equator (see Methods or Muri et al. (2018)⁵).

While numerous independent studies have confirmed the efficacy of RFG in limiting future global warming, e.g., keeping global mean temperature increase below 2 °C^{5,15,16}, others have found undesirable effects on climate conditions and related ecosystem effects under RFG implementation. Such undesirable effects include changes in precipitation patterns¹⁷, monsoon periods¹⁸, crop yields¹⁹, altered ocean productivity²⁰, enhanced ocean acidification²¹ and dryland expansion²². A few studies have focused on the Arctic cryosphere or ecosystem response under RFG, mostly focusing on the effects of SAI on sea ice or permafrost. While one study found that sea ice extent still decreases under two different SAI approaches, although not as quickly as under their reference scenario²³, another found that SAI can remediate sea ice cover by mid-century, but that large, sustained emission of SO₂ would be required²⁴. Other studies analysed the most beneficial timing of SO₂ injection to achieve the highest restoration of sea ice per unit of injection, finding that injecting SO₂ at 60°N during spring leads to peak aerosol depth in the summer²⁵. Another study analysed the response of permafrost warming under two different SAI scenarios applied to the RCP8.5 emission scenario, concluding that SAI slows down the warming of permafrost but not to the level of RCP4.5²⁶. Several studies have shown that equatorial-injected SAI and MCB tend to cool the Arctic less than the global mean by the nature of their design, as they are mainly applied over the tropics and mid-latitudes (e.g. refs. 27,28). However, there is a lack of thorough analysis on how different RFG methods will impact high-latitude ecosystems, especially considering extreme temperatures. Generally, polar regions have not been the centre of attention in RFG studies. We emphasise the importance of polar regions, not only due to the amplified climate change they are undergoing²⁹, but also due to their climate and ecological teleconnections to mid-latitudes^{30,31}, which play an important role in controlling the Earth's climate³². It is crucial to understand the potential side effects of RFG on the Arctic and how RFG might alter the Arctic climate and ecosystems.

RFG would cool the Earth by offsetting the radiative forcing from CO₂, but would not directly downregulate the high CO₂ concentration in the atmosphere. In addition to its greenhouse warming effect, CO₂ indirectly

influences the climate through its impact on plant physiology, with the two main processes being CO₂ fertilisation and stomatal closure which have opposite effects on transpiration³³. The two processes are often summarised under the term plant physiological forcing. The CO₂ fertilisation effect was found to be dominant over changes in temperature, precipitation and radiation for tropical forests in MCB simulations³⁴, increasing the rate of photosynthesis and hence the productivity and growth of plants³³. Simulations suggest that CO₂ fertilisation explains 70% of the observed increase in Leaf Area Index³⁵ which in turn increases the total transpiration from plants³⁶. Stomatal closure, on the other hand, describes the process of plants closing their stomata under elevated CO₂ concentrations to reduce water loss, therefore reducing transpiration³⁷. Recent studies suggest this process can remotely influence Arctic temperatures through enhanced heat transport from mid-latitudes towards the pole, introducing additional positive feedback and contributing to Arctic amplification³⁸. This can lead to changes in extreme temperatures and heatwaves³⁹, as well as processes that could cause additional feedbacks such as increased wildfire frequency or permafrost thaw. The interplay between increased plant physiological forcing under unabated anthropogenic CO₂ emissions and the potential application of RFG in the future is poorly understood and represents a key knowledge gap in RFG research. It is crucial to understand how RFG impacts CO₂-related processes, such as plant physiological forcing, that are not controlled by geoengineering management, especially in a region like the Arctic that is not only heavily impacted by plant physiological forcing through heat transport³⁸, but has also been shown to be one of the most impacted regions by global warming³².

Here we assess how RFG methods affect the Arctic, focusing on changes in the surface energy balance and extreme events, based on the fully coupled NorESM1-ME simulations^{5,19,21}. The three RFG methods are implemented in the model such that they reduce the radiative forcing of the representative concentration pathway with 8.5 W m⁻² radiative forcing (RCP8.5) to 4.5 W m⁻² (RCP4.5) by 2100. The NorESM1-ME simulation experiment has been shown to succeed in reducing the radiative forcing by 4 W m⁻² and controlling global mean temperatures, keeping them close to the level of RCP4.5⁵. To analyse extreme events, we firstly assess monthly boreal summer (JJA) maximum temperature (T_{Xx}), boreal winter (DJF) minimum temperature (T_{Nn}) and mean temperature (T_{mean}) over land. Surface warming due to physiological forcing was previously found to be the highest over mid- to high-latitudes³⁸, with the excess surface heat energy being transported to the Arctic region, which is why we analyse not only the area >65°N, but also >50°N. To investigate the impact of plant physiological forcing on temperature extremes in the Arctic, we analyse the regional energy budgets and evaluate potential shifts in the flux partitioning at the end of the century compared to RCP4.5 in a second step. Since CO₂ is not controlled by RFG, the atmospheric CO₂ concentration under RFG is the same as under RCP8.5. We therefore expect the stomata to close, releasing less water and inducing a shift in energy balance partitioning away from latent heat and towards sensible heat. For this, we analyse the change in different climate variables with global warming under RCP4.5, RCP8.5 and RFG (T_{glob} , Supplementary Fig. 1). Lastly, we connect the RFG-induced changes in climatic conditions to Arctic terrestrial system dynamics, such as burned area and permafrost temperature conditions.

In this study, we show that while the three analysed RFG methods succeed in cooling the global climate to the temperature level of RCP4.5, Arctic temperatures are much less controlled. We find that Arctic extreme temperatures, particularly maximum temperature under CCT and MCB and minimum temperature under SAI, are increased as compared to RCP4.5. Compared to the first 21 years of RCP8.5, the Arctic is 4.4–4.7 °C warmer by the end of the century under all three RFG methods—0.7–1.1 °C more than under RCP4.5 (Supplementary Fig. 2b). We show that all three RFG methods have reduced transpiration as compared to RCP4.5 by the end of the century, indicating stomatal closure. Our results show that achieving a 2 °C global mean temperature goal under the three RFG scenarios simulated here results in a worse outcome for Arctic climate extremes than if the same

temperature target was achieved under RCP4.5, such as with emissions mitigation.

Results

Extreme temperatures in the Arctic are less controlled under RFGs

As was shown in a previous study using the same simulation output⁵, all three geoengineering experiments show end of the century near surface air temperatures close to but slightly above RCP4.5 (CCT is 0.28 °C, MCB is 0.25 °C and SAI is 0.40 °C higher than RCP4.5) (Supplementary Fig. 1). This has previously been attributed to RFG being applied only in 2020, when RCP8.5 and RCP4.5 have already been simulated differently since 2006 and additional heat could accumulate under RCP8.5⁵. MCB and SAI were both able to achieve the desired negative radiative forcing of -4 W m^{-2} at the end of the century, but only -3.8 W m^{-2} could be achieved within this modelling setup with CCT⁵. CCT has a higher surface direct visible solar radiation while MCB and SAI are designed with a lower surface direct visible solar radiation than RCP4.5 and RCP8.5. In contrast, SAI and MCB show higher diffuse visible solar radiation, while CCT has a lower diffuse visible solar radiation than both RCP scenarios⁵.

While the absolute monthly temperatures in the Arctic are below RCP8.5 under RFG, none of the RFG experiments succeed in cooling the region north of 50°N and the Arctic region to the temperature level achieved under RCP4.5 (Supplementary Fig. 2). North of 50°N, the mean temperature of land is 1.01 °C higher under CCT, 0.94 °C higher under MCB and 0.88 °C higher under SAI compared to the RCP4.5 scenario. In the Arctic, the mean temperature of land is 0.91 °C higher under CCT, 0.74 °C higher under MCB and 1.05 °C higher under SAI compared to the RCP4.5 scenario. Since global mean temperature is not completely restored to RCP4.5, we also analyse the response of the regional mean temperature (T_{mean}) to increases in global mean temperature (T_{glob} ; Fig. 1a), which enables the comparison of the Arctic temperatures under RCP and RFG at a particular target global mean temperature. In the region north of 50°N, RCP8.5, RCP4.5 and SAI show similar linear increases in T_{mean} with T_{glob} . In the same region, CCT and MCB show a slightly higher increase in T_{mean} with T_{glob} . This means that under a certain global mean temperature increase target (e.g., 2 °C), the mean temperature increase of the region north of 50°N will be higher under CCT and MCB than under RCP8.5, RCP4.5 and SAI.

Both CCT (1.62 °C) and MCB (1.48 °C) show an increased anomaly in boreal summer maximum temperature (T_{Xx}) in the region north of 50°N. Under SAI this region experiences an increase in boreal winter minimum temperature (T_{Nn}) of 1.49 °C compared to RCP4.5 by 2100. This difference in T_{Nn} is even more pronounced when only considering the Arctic (1.81 °C by 2100). We show that under RFG (excluding SAI), the increase in T_{Xx} per increase in T_{glob} is even more amplified when compared to the two RCP scenarios north of 50°N (Fig. 1b). This shows that even if global mean temperatures were completely restored to RCP4.5, the maximum temperature in the region north of 50°N would still be considerably higher in the three scenarios analysed here than under RCP4.5. Contrary to T_{Xx} , the three

different RFG methods do not show significant differences in T_{Nn} north of 50°N (Fig. 1c). In the area north of 65°N, T_{Nn} shows the strongest increase per °C increase in T_{glob} under SAI (Supplementary Fig. 3). This implies that SAI is not as effective in cooling down minimum temperatures in high latitudes. This has been previously established and attributed to the latitudinal temperature gradient, with lower latitudes cooling more than higher latitudes under SAI injected at the equator (see also Supplementary Fig. 12), especially during the polar nights when there is no solar radiation to reflect and an increased equator-to-pole temperature gradient in the stratosphere^{4,40,41}.

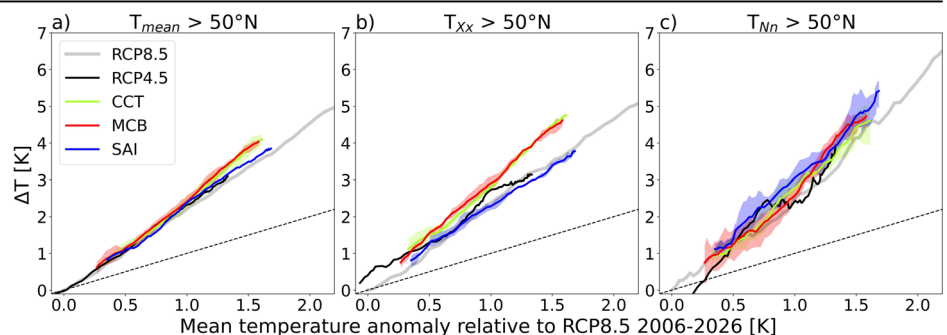
The spatial pattern of T_{Xx} differences between RFG and RCP4.5 per unit T_{glob} increase (see Methods: Statistical Analysis) shows the strongest increases in the Northern Hemisphere under CCT and MCB (Supplementary Fig. 4a, b). This indicates that under CCT and MCB, T_{Xx} is increasing more with T_{glob} than under RCP4.5 in mid- and high-northern latitudes. SAI has less consistent deviations from RCP4.5 in T_{Xx} , indicating regions where T_{Xx} is increasing more with T_{glob} under SAI than under RCP4.5 and other regions where T_{Xx} is increasing less with T_{glob} (Supplementary Fig. 4c). When considering the T_{Nn} increase per increase in T_{glob} , the three RFG scenarios show a similar pattern with an increase in the linear regression (LR) slope compared to RCP4.5 in Eurasia and most parts of North America and a decrease in Alaska, Greenland and eastern Siberia (Supplementary Fig. 5). The differences between methods seen in Fig. 1 where SAI shows a higher increase in T_{Nn} with T_{glob} than the other methods, can be attributed to both CCT and MCB showing regions where the increase in T_{Nn} with T_{glob} is substantially lower than under RCP4.5, compensating for areas with a higher increase when considering the whole Arctic land region.

Change in energy budget components

Due to the closing of plant stomata to conserve water under high CO_2 concentration environments, we expect changes in the energy budget resulting from plant physiological forcing. As the RFG methods do not directly and notably alter the terrestrial and oceanic carbon sinks⁵, they simulate a similar atmospheric CO_2 increase as RCP8.5, subsequently increasing the effect of plant physiological forcing in the future compared to the lower emission scenario RCP4.5⁴². Previous studies confirmed that stomatal closure leads to less transpiration, as the plants close their stomata to preserve water, increasing the ratio of sensible to latent heat (also known as Bowen ratio) and subsequently increasing surface temperatures^{33,43,44}, which can explain the difference in mean and extreme temperature shown in Supplementary Fig. 2. We find that per unit T_{glob} increase the transpiration amount was significantly reduced under all three RFG methods in high-latitudes relative to RCP4.5 during boreal summer (Fig. 2a, d, g). We also see an increased ratio under all three RFG methods compared to RCP4.5 in 2100 in the land region north of 50°N (Fig. 3), which is expected with decreased transpiration and suggests increased stomatal closure.

While we observe reduced transpiration as compared to RCP4.5 during boreal summer in the region north of 50°N under all three RFG methods, the expected increase in sensible heat following reduced

Fig. 1 | Simulated temperature anomaly in RCP8.5, CCT, MCB and SAI from 2006–2026. Anomaly in (a) mean (T_{mean}), (b) maximum (T_{Xx}) and (c) minimum (T_{Nn}) land temperature north of 50°N (y-axis) compared to the global mean temperature (T_{glob}) anomaly over land and ocean (x-axis). The anomalies are respective to the mean of RCP8.5 from 2006–2026 and are shown for RCP8.5 (grey), RCP4.5 (black), CCT (lime), MCB (red) and SAI (blue). The lines represent the respective ensemble mean. The ensemble spread is shaded. The hatched line represents the 1:1 line.



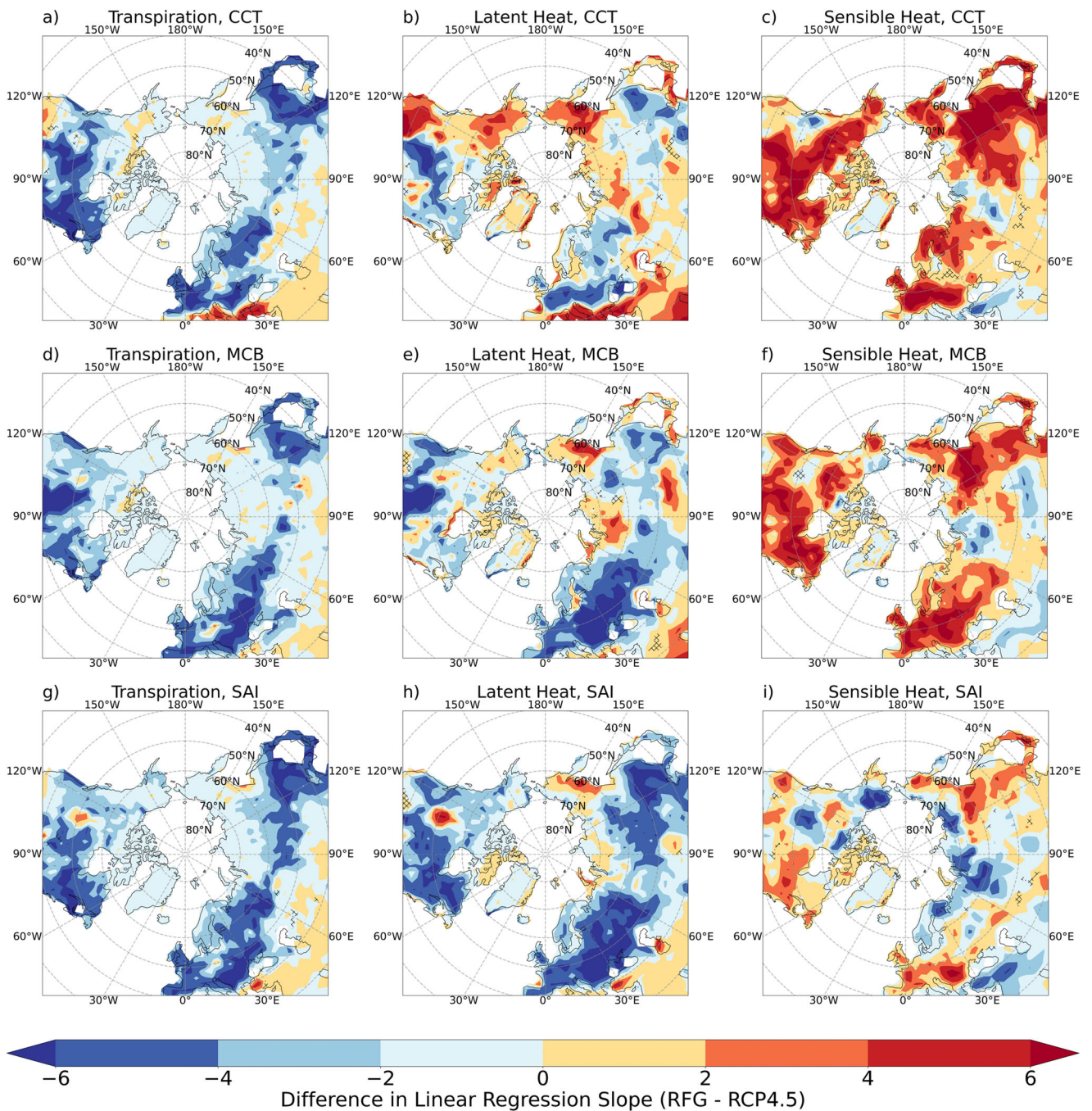


Fig. 2 | Simulated change in regression slope of transpiration, latent heat and sensible heat in the Arctic against global mean temperature under CCT, MCB and SAI during boreal summer. Pattern of the difference between the respective RFG scenarios and the RCP4.5 scenario in the linear regression slope between

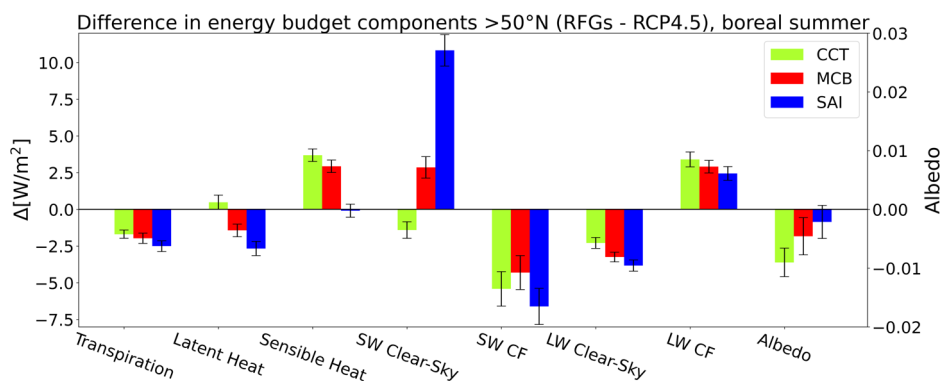
transpiration (a CCT, d MCB, g SAI), latent heat (b CCT, e MCB, h SAI) and sensible heat (c CCT, f MCB, i SAI), respectively and T_{glob} . The hatching indicates insignificant differences at the 95% confidence level.

transpiration in 2100 is seen in CCT and MCB, not in SAI (Fig. 2a–i). Increased sensible heat has been shown in previous studies to increase boundary layer temperatures^{45,46} and the intensity and frequency of heatwaves^{47,48}. Of the three RFG methods, CCT is the only method that shows slightly increased latent heat in 2100 in the region north of 50°N during the boreal summer (Figs. 2b, 3), indicating a strengthened hydrological cycle⁴⁹. This is also illustrated in the precipitation pattern, where CCT generally shows a higher increase in precipitation with global warming north of 50°N during boreal summer compared to RCP4.5 (Supplementary Figs. 6, 8b). This is consistent with soil moisture patterns, where all three RFG methods show a lesser decrease with warming than RCP4.5

(Supplementary Figs. 7b, 8a). This result is consistent with previous modelling studies that found an increased latent heat flux when applying CCT and attributed this change to increased radiative cooling in the troposphere caused by thinning of cirrus clouds⁴⁹.

SAI shows the largest deviation from RCP4.5 in soil moisture out of all three RFG methods, which cannot solely be explained by precipitation when considering the pattern of precipitation under SAI (Supplementary Fig. 6c). SAI, however, also shows substantially larger decreases in ground evaporation with global warming, compared to RCP4.5, therefore increasing the soil moisture (Supplementary Fig. 7e). Regions showing a decrease in precipitation per unit of global warming under SAI compared to RCP4.5

Fig. 3 | Difference between RCP4.5 and RFG in surface energy budget components over land north of 50°N in boreal summer in 2080–2100. Difference of the energy budget components >50°N in 2080–2100 of the RCP4.5 scenario (0-line) and CCT (lime bars), MCB (red bars) and SAI (blue bars). For albedo, the right y-axis applies; all other variables are plotted on the left y-axis. The skewers indicate 95% confidence intervals. Incoming surface fluxes are defined as negative, outgoing surface fluxes as positive. SW shortwave, LW longwave, CF cloud forcing.



with an increase in soil moisture (i.e., northern continental Canada) match well with regions where the snow cover decreases less with global warming (positive difference) compared to RCP4.5 when considering the whole year (Supplementary Fig. 9f), indicating that part of the difference in soil moisture under SAI is due to snow melt. While SAI does show an increased ratio of sensible to latent heat during boreal summer, as expected through physiological forcing, sensible heat is reduced compared to RCP4.5, indicating decreased boundary layer temperatures and explaining why SAI shows a different pattern in T_{xx} (Fig. 1b).

SAI further shows significant differences to CCT and MCB when considering the shortwave radiation north of 50°N in 2100 during boreal summer (Fig. 3). While we find a decreased shortwave cloud forcing of similar magnitude in all three RFG scenarios compared to RCP4.5, the clear-sky shortwave radiation significantly differs between them. As MCB is applied in NorESM1-ME between the latitudes of 45°S and 45°N, we would not expect a difference from the other RFG methods in shortwave cloud forcing north of 50°N. While SAI also targets shortwave radiation, the mechanism is based on increased aerosol optical depth in the stratosphere and not on cloud albedo, hence no change in shortwave cloud forcing is expected directly from the treatment either. Our result shows a significant decrease in incoming clear-sky shortwave radiation at the surface in the Arctic region for SAI caused by the increased aerosol optical depth in the stratosphere. In Fig. 3, we define outgoing surface fluxes as positive while incoming surface fluxes as negative. Hence, positive fluxes imply a cooling of the Earth's surface, whilst negative imply a warming. The positive sign in shortwave radiation in SAI thus signifies a surface cooling effect through a decreased incoming shortwave flux. The effect of the aerosols on the radiation becomes clearer when analysing changes in the surface albedo under the three RFG scenarios in the Arctic (Fig. 3). The albedo under SAI in the Arctic during boreal summer is the closest to that of RCP4.5 and therefore not significantly different, while CCT and MCB show a significant decrease in albedo. The decreased albedo in CCT and MCB can be explained by the decrease in snow cover fraction during boreal summer (Supplementary Fig. 10b). This difference in albedo is an explanation for why SAI shows such different responses in maximum temperature when compared to CCT and MCB as it leads to less incoming shortwave radiation, offsetting the effect of decreased transpiration and increased ratio of sensible to latent heat and hence decreasing the warming and risk for heatwaves that we hypothesised in Fig. 1b for CCT and MCB.

Impacts on Arctic system dynamics

Lastly, we assess how shifts in temperature extremes and surface energy budget affect the projected burned area and permafrost temperature conditions in the Arctic. Previous studies showed that fire frequency increases under hot and dry conditions^{50–52}, and Arctic fires are particularly sensitive to boreal summer temperatures^{50,51} and anomalously warm periods⁵³. We have already shown that under CCT and MCB, maximum summer temperature increases more with T_{glob} than RCP8.5, RCP4.5 and SAI (Fig. 1), potentially leading to climatic conditions more

conducive to fire activity in the Arctic. The analysis of the MODIS burned area satellite dataset⁵⁴ in combination with the temperature data from Climatic Research Unit TS4.01⁵⁵ shows that the majority of fire events occur when T_{xx} anomalies are higher than T_{mean} anomalies (Fig. 4a). The simulated temperature frequency distribution in 2100 under the RCP4.5 scenario shows most T_{xx} and T_{mean} combinations occur when T_{xx} anomalies are similar to T_{mean} anomalies (Fig. 4b), but under CCT and MCB, the frequencies change slightly so that T_{xx} anomalies are higher than T_{mean} anomalies (Fig. 4c, d). This means higher T_{xx} anomalies are simulated under CCT and MCB under given T_{mean} anomalies than under the RCP4.5 simulation—especially for T_{mean} anomalies of around 3 °C. The narrowing of the temperature conditions under CCT and MCB is due to three CCT and MCB simulations with slight perturbations to initial conditions being carried out and averaged while RCP4.5 was only simulated once. This shows the internal variability of the model, where ensembles with slightly different initial conditions lead to slightly different simulation outcomes. Taking the average of the three ensembles reduces variability in the temperature anomalies. Contrary to Fig. 4, we did not take the mean of the ensembles in Fig. 5, hence keeping the variability of the RFG simulations similar to the RCP4.5 simulation. Fig. 5 confirms what we see in Fig. 4: while the difference in T_{xx} anomaly and T_{mean} anomaly in 2100 is around 0 under RCP4.5 (0.06), both CCT (0.69) and MCB (0.70) show a slight change towards T_{xx} anomalies that are higher than T_{mean} anomalies (Fig. 5). These conditions are favourable conditions for the burned area as we have shown in Fig. 4a. This result suggests that temperature conditions under CCT and MCB shift towards conditions where the burned area is larger than under RCP4.5 by the end of the century. Since wildfires are also heavily impacted by hydrological conditions⁵⁰, the fire weather index metrics, which includes meteorological conditions, are used. Due to the temporal constraint of our data, this analysis is not possible for this study. We do, however, see that particularly under MCB, precipitation is significantly decreased in large areas of the Arctic (Supplementary Figs. 6, 8), especially central and eastern Siberia. This is also reflected in the soil moisture (Supplementary Figs. 7, 8), where MCB shows a lower soil moisture than RCP8.5 in central and eastern Siberia. Both decreases in precipitation and soil moisture are additional factors increasing the likelihood of wildfires. CCT shows a more mixed signal than MCB with some regions experiencing less precipitation and lower soil moisture while others experience more precipitation and higher soil moisture than under RCP4.5. Overall, precipitation is thought to increase under CCT⁴⁹, which would decrease the likelihood of wildfires.

Permafrost thawing may accelerate global-scale warming by releasing large amounts of organic matter storage⁵⁶ as greenhouse gas emissions⁵⁷. We hypothesise that permafrost may continue to thaw with the strong increase in the minimum temperatures over several years. We focus on SAI to test this hypothesis as SAI is the only scenario where boreal winter minimum temperatures north of 65°N differ from the other scenarios (Supplementary Fig. 3). The current distribution of permafrost fraction⁵⁸ against temperature

Fig. 4 | Change in JJA maximum temperature frequency in CCT and MCB related to fire frequency north of 50°N. a Conditions under which fires are currently observed in the Arctic^{54,55}. The anomalies are calculated to 2001–2020. **b** Maximum temperature frequency north of 50°N of RCP4.5 in 2080–2100. Difference of the maximum temperature frequency between CCT (c) and MCB (d) in 2080–2100 and RCP4.5 in 2080–2100. The hatched line represents the 1:1 line.

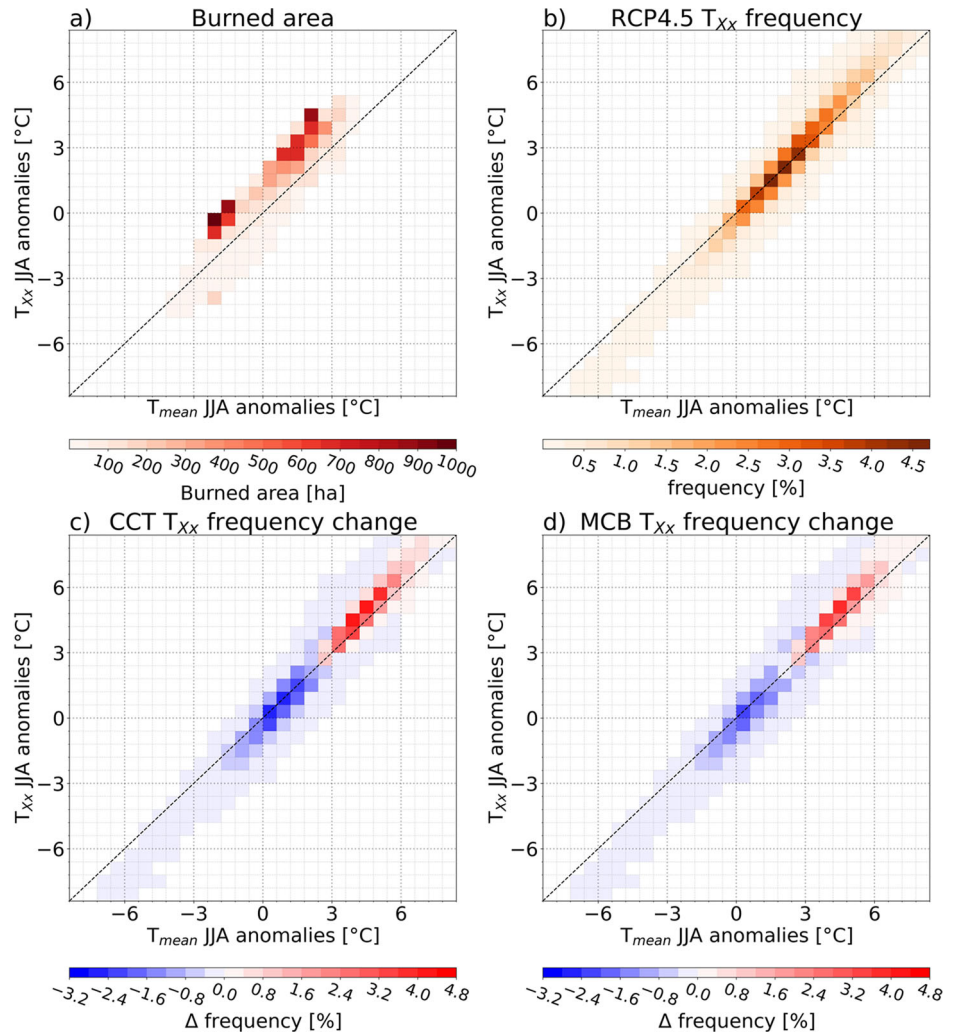
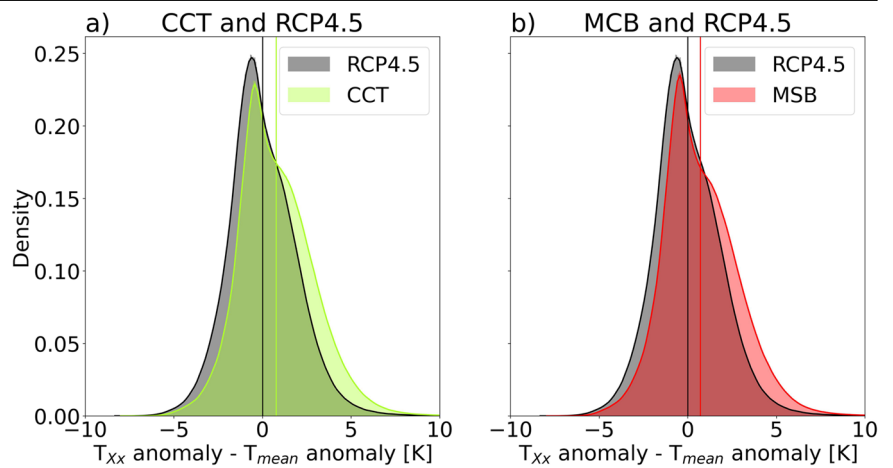


Fig. 5 | Histograms of difference in JJA T_{xx} anomaly and JJA T_{mean} anomaly under CCT, MCB and RCP4.5 north of 50°N. The anomalies are calculated for RCP4.5 (grey), (a) CCT (lime) and (b) MCB (red) between 2080–2100 for each grid cell from daily datasets compared to RCP4.5 2006–2026 of the respective grid cell. The vertical lines represent the mean of the respective scenario.

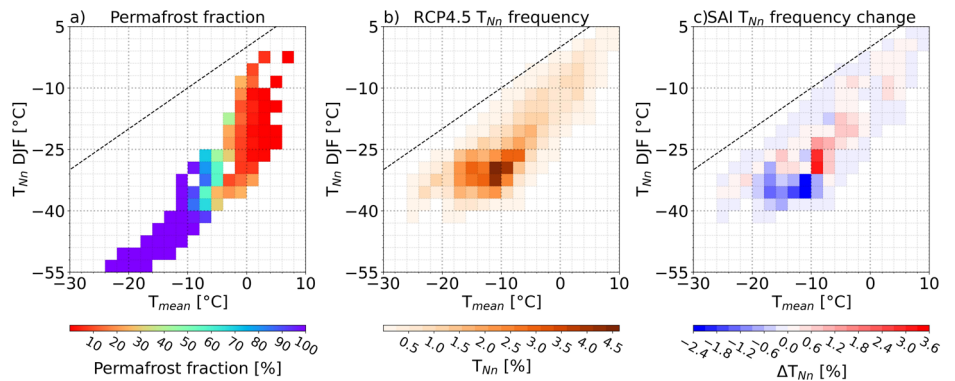


conditions⁵⁵ (T_{mean} versus T_{Nn}) shows that the permafrost fraction is highest below $-10\text{ }^{\circ}\text{C}$ T_{mean} and is more variable to T_{Nn} for T_{mean} ranges around $-5\text{ }^{\circ}\text{C}$ where small changes in T_{Nn} can cause large changes in permafrost fraction (Fig. 6a).

The permafrost area extent modelled for the first 21 years of RCP4.5 shows a negative linear relationship with T_{Nn} (Supplementary Fig. 11). The T_{Nn} frequency distribution of RCP4.5 in 2100 shows that the maximum

frequency distribution occurs between $-15\text{ }^{\circ}\text{C}$ T_{mean} and $-30\text{ }^{\circ}\text{C}$ T_{Nn} (Fig. 6b). We notice that under SAI the region of the highest frequency of T_{Nn} conditions shifts towards higher minimum temperatures, where temperature conditions are more favourable for permafrost degradation (Fig. 6c). The maximum difference in T_{Nn} is around $-10\text{ }^{\circ}\text{C}$ T_{mean} , where the permafrost fraction might be particularly sensitive to T_{Nn} . While under RCP4.5 2,120,064 km^2 of the area is permanently frozen for at least 2 years

Fig. 6 | Change in DJF minimum temperature frequency in SAI related to permafrost north of 65°N. a Conditions under which permafrost is currently observed in the Arctic⁵⁸. **b** Minimum temperature frequency north of 65°N of RCP4.5 in 2080–2100. **c** Difference of the minimum temperature frequency SAI in 2080–2100 and RCP4.5 in 2080–2100. The hatched line represents the 1:1 line.



(T_{mean} below 0 °C for 24 consecutive months), this decreases by 7.78% to 1,955,148 km² under SAI at the end of the century. Our results indicate that under SAI, the climatic conditions in the Arctic will be less favourable for permafrost when compared to RCP4.5 in 2100.

Discussion and conclusion

While equatorial SAI and to a lesser extent MCB are expected to result in a latitudinal temperature gradient with lower latitudes cooling more than high latitudes⁴ (see also Supplementary Fig. 12), this study further confirms the undercooling of the Arctic under all three RFG scenarios analysed here. This is not a RFG specific problem, as Arctic amplification has been widely established²⁹. We further find that (i) CCT and MCB have a slightly higher Arctic amplification than RCP4.5 and (ii) Arctic maximum temperature under CCT and MCB and Arctic minimum temperature under SAI are less controlled than the global mean temperature. Our results show that reaching the 2 °C global mean temperature target under these three RFG scenarios leads to less favourable temperature conditions in the Arctic than achieving this target by reducing CO₂ emissions. The Arctic mean temperature is more than 4 °C higher in 2080–2100 under the three RFG designs analysed here than in the 2006–2026 mean of RCP8.5. Further, the Arctic is 0.7–1.1 °C warmer at the end of the century under the three RFG methods than under RCP4.5, has been shown in previous studies for equatorial SAI and MCB and has been explained with the latitudinal gradient that originates from the non-homogeneous application forcings applied in our methods^{27,28}. We find that the extreme temperatures T_{Xx} and T_{Nn} in the Arctic are considerably higher under RFG than under RCP4.5 and differ between the methods. Previous studies confirm this finding for SAI, indicating T_{Nn} in the Arctic is considerably higher than in other regions and attributed this mainly to enhanced poleward transport of energy and direct longwave heating of the surface from increased CO₂ and atmospheric water vapour^{41,59}. Because of the lack of solar radiation in boreal winter across the Arctic, SAI might only have a limited impact on cooling in the polar winter⁴¹; however, it might have indirect effects from connections with other regions, climate feedback and circulation changes³⁸. Additionally, due to stratospheric heating caused by the longwave absorption of the injected aerosols (compare Supplementary Fig. 12), large scale atmospheric dynamics are altered under SAI. Ref. ⁶⁰, for example, studied the response of atmospheric dynamics under different injection strategies. For equatorial injection they found a strengthening of the polar vortex which ultimately caused winter warming over large parts of the European and American Arctic, similar to our findings. CCT and MCB are not as well researched as SAI and hence their impact on global circulation patterns is less known. In our simulations, MCB shows few-to-no significant changes from RCP4.5 in tropospheric temperatures and the stratospheric temperatures are similar to RCP8.5. CCT shows a cooling in the higher equatorial troposphere and a heating in the stratosphere just above. This might be due to a reduced flux of water vapour from the troposphere into the stratosphere⁶¹. We show that all three of the presented RFG methods could introduce additional risks to the Arctic terrestrial system compared to RCP4.5 by the end of the century.

The changes observed in the energy budget components in CCT and MCB support the hypothesis that the increase in T_{mean} and T_{Xx} in the Arctic can be linked to plant physiological forcing. SAI does not deviate significantly from RCP4.5 in T_{Xx} . While the decrease in transpiration and increased ratio of sensible to latent heat indicates enhanced plant physiological forcing for all three RFG methods, the effect in boreal summer under SAI is potentially offset due to changes in shortwave radiation, leading to higher surface albedo as compared to the other RFG methods (Fig. 3). We note that the experimental setup of this study was not designed to test for physiological forcing directly, as the study by Park et al. (2020) was³⁸. Hence, we cannot rule out other potential factors for changes in transpiration such as precipitation and temperature. Nonetheless, there is a shift from latent to sensible heat under all three RFG methods compared to RCP4.5, increasing the atmospheric surface temperature and indicating plant physiological forcing³⁸. A previous study has shown that plant physiological forcing accounts for roughly 15% of the trend of increasing maximum temperatures with increases in CO₂ and that particularly in high latitudes the increase in T_{Xx} is higher than in T_{mean} , similar to our findings³⁹. Further research is needed to better understand the effect RFG can have on the Arctic region, especially considering the different effects they have on the energy budget and to analyse the underlying mechanisms.

Our results show that the three RFG methods analysed here lead to climatic conditions favouring more fire activity under CCT and especially MCB when including changes to the hydrological cycle. Under equatorial SAI, temperature conditions are more favourable for permafrost degradation, than under RCP4.5. While there are other factors affecting fire occurrence in relation to RFG (e.g., soil moisture, lightning frequency or human-caused ignition), the shift in climatic conditions is an indication of increased fire activity in the Arctic under CCT and MCB. Both wildfires⁶² and permafrost thaw⁵⁶ are huge sources of carbon, emphasising why it is crucial to understand how the conditions for extreme events will change under RFG management.

The RFG methods evaluated here are currently not understood enough to advocate for practical implementation. Many studies highlight the uncertainties and risks that come with implementation. We find that whilst RFG methods could effectively cool down the Earth's mean temperature, they also show undesirable side effects, such as changes to precipitation patterns and extreme temperatures and therefore must be handled with care.

NorESM1 has been shown in several model intercomparison studies to be generally consistent with the observed temperature trends^{63,64}. Models of the Climate Model Intercomparison Project (CMIP5) have typically been shown to overestimate the surface cooling following volcanic eruptions⁶⁵, which would impact their response to SAI as well. However, NorESM1-ME has been shown to simulate the surface temperature response to volcanic eruptions well⁶⁴. As has been shown by e.g. ref. ⁶³, the accuracy of modelled contemporary warming trends correlates well with projected future warming sensitivity. Further, ref. ⁶⁴ show that the response of global cooling under SAI is strongly related to the individual model-dependent simulated

cooling during historical volcanic eruptions. In both studies, NorESM1 has been shown to be consistent with the observed temperature trends, subsequently having more reliable future projections.

NorESM1 does simulate a relatively strong Atlantic Meridional Overturning Circulation (AMOC) which is a potential explanation for the lower-than-average mean surface air temperature compared to other CMIP5 models⁶⁶. Ref. ⁵ have analysed changes in the AMOC after RFG deployment with the same datasets analysed here. While the AMOC is simulated to substantially weaken more under RCP8.5 than under RCP4.5, all three RFG scenarios have been found to restore the AMOC close to the RCP4.5 levels⁵. Considering the model's relatively strong initial AMOC, it is likely that the AMOC would be weaker than predicted in all scenarios (RCP8.5, RCP4.5 and RFGs). By isolating the effects of a weakened AMOC, ref. ⁶⁷ have shown that the warming magnitude in the Arctic could be even larger without AMOC slowdown. Hence, a weaker AMOC in all scenarios could potentially lead to a cooler Arctic in all scenarios. Future corresponding studies that apply models with weaker mean AMOC state would be valuable to confirm this.

Although the concentration driven model of NorESM1, NorESM1-M, has been shown to be a valuable global climate model⁶⁶ and is part of the Geoengineering Model Intercomparison Project (GeoMIP)⁶⁸ and the CMIP5⁶⁹, the limitation of only using one Earth System Model must be noted. CCT in particular seems dependent on the increase in ice crystal fall speed chosen, as a study has found that the Arctic is particularly well cooled under CCT, contrary to our results⁷⁰. The assessment of the impact of plant physiological forcing under RFG would greatly benefit by including the comparison of multiple Earth System Models. Furthermore, it is known that the Arctic has higher uncertainties in climate projections than any other region since quantitative understanding of the feedback between the physical processes in the Arctic system is currently still lacking⁷¹. Recent studies have shown that combined forcings of CO₂ and anthropogenic aerosols can lead to substantial regional nonlinear effects in the climate system, especially in the Arctic region⁷². This adds an additional layer of uncertainty to the assessment presented in this study. In this regard, future studies that assess the impact of RFG in the absence of other external forcings could be valuable. An additional constraint comes from the temporal resolution of the model. Most model output variables of our geoengineering experiments are only provided in monthly resolution. Future fire analyses would benefit from using daily values enabling the calculation of the fire weather index, combining different weather factors contributing to the likelihood of fires as well as duration of extreme events.

The model design and simulation were carried out when injecting SO₂ close to the equator was the dominant strategy for SAI. New studies have proposed new injection strategies, like placing several injections in the tropics that reduce some of the adverse effects of SAI⁷³. Others have proposed high latitude-specific SAI by injecting at 60°N, which would reduce the under-cooling of high northern latitudes⁴¹. This has been shown to reduce permafrost thaw, restore September sea ice and reduce the Greenland Ice Sheet runoff, but also cause a southward shift of the Intertropical Convergence Zone, highlighting that this would not be local geoengineering only affecting the Arctic²⁵. An injection further north has the potential to alleviate the effect of minimum temperature being less controlled under SAI, as highlighted in this study, although there are no studies so far showing the effects of Arctic SAI on minimum temperatures.

There is no clear estimation for the costs of an actual RFG implementation, as it would have to be carried out for as long as it takes to reduce the CO₂ concentration in the atmosphere. Without reducing the CO₂ in the atmosphere, RFG would need to be continued forever, as a sudden stop would cause the climate to rapidly revert to that without RFG methods^{5,22}, leaving no time for ecosystems to adapt. Future research is needed to understand the influence of RFG on climate extremes in ecosystems and how it impacts the socioeconomic system. Our results suggest that, while for a given emissions pathway (in this case RCP8.5) RFG could reduce the climate risk, it does not succeed at lowering the temperatures in the Arctic to those of RCP4.5 and that RFG

applications under high CO₂ future scenarios pose more risks than emissions reduction. More studies are required to assess the impact of RFG under mitigated scenarios. Our study helps to understand better the potential risks that come with RFG, however, many uncertainties about the deployment of RFG remain.

Methods

Model description

To assess the influence of RFG on the Arctic terrestrial systems, we use the fully coupled, emission driven Norwegian Earth System Model (NorESM1-ME) described in detail by ref. ¹³ and ref. ¹⁴. NorESM1 is based on the Community Climate System Model version 4 (CCSM4). Changes relevant for this analysis include a (1) modified chemistry-aerosol-cloud-radiation scheme⁷⁴ and (2) coupling of the ocean carbon cycle model with an isopycnic ocean general circulation model¹³. The model was included in phase 5 of the CMIP5⁶⁹ and the Geoengineering Model Intercomparison Project (GeoMIP)⁶⁸. It has a resolution of 1.9° latitude by 2.5° longitude and 26 vertical layers¹³. The variables used in this analysis are summarised in Table 1.

The land model used in NorESM1 is version 4 of the Community Land Model (CLM4) of CCSM4^{75,76}. The model includes 24 plant functional types (PFTs), differing, among other factors, in leaf and stomatal optical properties that determine reflection, transmittance and absorption of solar radiation, as well as photosynthetic parameters that determine stomatal resistance, photosynthesis and transpiration. The main Arctic PFTs are divided into needleleaf evergreen tree boreal, needleleaf deciduous tree boreal, broadleaf deciduous tree boreal, broadleaf deciduous shrub boreal and C3 Arctic grass. Stomatal conductance is modelled from the Ball-Berry conductance model that relates stomatal conductance to net leaf photosynthesis, scaled by relative humidity and the CO₂ concentration at the leaf surface. A more detailed description of the model and applied theorems is described in ref. ⁷⁵.

NorESM1-ME uses a spatially- and annually-varying prescribed vegetation cover following the CMIP5 global land use and land cover change dataset⁷⁷. The transient PFT and land cover fields take historical and future climate change under the RCP8.5 scenario (1850–2100) into account, which were derived using the global land model offline and Integrated Assessment Model, respectively^{5,21}. The model uses the default setting, which turns off the Dynamic Vegetation model. More details on PFT and land cover implementation in the CLM4 model are described in ref. ⁷⁸.

Table 1 | Description of the analysed variables

Name	Long Name
TS	Surface temperature (radiative) [K]
TSA	2 m air temperature [K]
TREFMXAV	Daily maximum of average 2-m temperature [K]
TREFMNAV	Daily minimum of average 2-m temperature [K]
FCTR	Canopy transpiration [W m ⁻²]
LHFLX	Surface latent heat flux [W m ⁻²]
SHFLX	Surface sensible heat flux [W m ⁻²]
FSNSC	Clear-sky net solar flux at surface [W m ⁻²]
FSNS	Net solar flux at surface [W m ⁻²]
FSDSC	Clear-sky downwelling solar flux at surface [W m ⁻²]
FLNSC	Clear-sky net longwave flux at surface [W m ⁻²]
FLNS	Net longwave flux at surface [W m ⁻²]
RAIN	Atmospheric rain [mm s ⁻¹]
QSOIL	Ground evaporation [mm s ⁻¹]
SOILLIQ	Soil liquid water [kg m ⁻²]
FSNOW	Fraction of ground covered by snow []

Radiative forcing geoeengineering scenarios

Three RFG methods are analysed here: CCT, MCB and SAI. They are designed to reduce the radiative fluxes at the top of the atmosphere from the RCP8.5 levels to that of the RCP4.5 scenario, requiring a radiative forcing of -4 W m^{-2} by 2100. RFG is applied for 81 years, starting in 2020. Three different ensembles are carried out for each RFG scenario, each with a small perturbation to initial conditions in the year 2020⁵. One simulation each is carried out for the RCP8.5 and RCP4.5 scenarios, running from 2006–2100.

CCT aims to thin high ice clouds, i.e., cirrus, that trap longwave radiation in the climate system and thus have a net warming effect. By thinning these clouds, more longwave radiation can escape to space, altering the Earth's radiation budget. This can be achieved by seeding ice nuclei in regions where cirrus clouds form to initiate heterogeneous freezing and the formation of larger crystals might fall out of the clouds, thereby thinning them out⁹. In NorESM1-ME, the method by ref. 79 is implemented: CCT is approximated by increasing the fall speed of crystals for temperatures colder than $-38 \text{ }^\circ\text{C}$ —the temperature where typically homogeneous freezing sets in. By increasing the number of particles, heterogeneous freezing can dominate and deplete the clouds of water vapour. The fall speed is increased by a factor of up to 10 by the end of the century.

MCB acts on the shortwave energy budget of the Earth system by enhancing the concentration of droplets in low marine stratocumulus clouds, increasing the cloud albedo. The suggested method is to inject ocean water mist into the lower atmosphere in regions where there is a deficit of cloud condensation nuclei (CCN), where the NaCl would function as CCN^{11,80}. The direct effect of the bright sea salt aerosols is also contributing to the cooling in the model, as established in ref. 10. NorESM1-ME contains a fully prognostic treatment of sea salt aerosol emissions as a function of sea surface temperatures and wind speed at 10 m above the surface⁸¹ and their coupling to cloud droplet number concentration⁵. MCB is implemented in NorESM1-ME according to the method of ref. 82 by increasing the natural emission of sea salt aerosols in the accumulation mode from the ocean surface to the lower atmosphere between the latitudes of 45°S and 45°N . NorESM1-ME was run with a fully prognostic treatment of cloud droplet number concentration (CDNC) and sea salt. The emissions of sea salt are increased uniformly over the seeding areas. The ambient conditions determine the amounts of sea salt that reaches the clouds and then serves as CCN. As the sea salt particle emission increases are done for the accumulation mode, the particles have a dry number modal radius of $0.13 \text{ }\mu\text{m}$, with a geometric standard deviation of 1.59, corresponding to a dry effective radius of $0.22 \text{ }\mu\text{m}$. To achieve the required -4 W m^{-2} in radiative forcing, the ocean area where CCN are emitted is increased as compared to Alterskjær and Kristjánsson (2013)⁸², who limited their area to $\pm 30^\circ$. By the end of the century, emissions of $\sim 460 \text{ Tg year}^{-1}$ of sea salt are required for the whole area⁵.

Similar to MCB, SAI affects the shortwave radiation budget of the Earth. SAI is the most studied RFG approach as it is based on the natural dimming following volcanic eruptions. In this approach, SO_2 is injected into the stratosphere, building a layer of aerosols that effectively scatter part of the incoming solar radiation, increasing the Earth's planetary albedo^{12,83}. The implementation of SAI in NorESM1-ME is according to the description of ref. 84: SO_2 is emitted into the stratosphere at a grid cell close to the equator at a height of around 20 km (60 hPa). The following evolution of SO_2 is simulated using an interactive aerosol microphysics module (HAM) of the general circulation model ECHAM5, which calculates the formation of sulphate aerosol, including nucleation, accumulation, condensation and coagulation processes⁸⁴. The same model setup has been used to simulate the 1991 Mt. Pinatubo eruption, showing a good representation of the particle size and global aerosol load⁸⁵. Ref. 5 found that the needed emission strength to offset 4 W m^{-2} radiative forcing requires $5 \text{ Tg(S) year}^{-1}$ in 2050, increasing to $10 \text{ Tg(S) year}^{-1}$ in 2075 and $20 \text{ Tg(S) year}^{-1}$ in 2100.

Experimental design

Our focus is to compare the RFG methods to the RCP4.5 scenario at the end of the century (2100). If not stated otherwise, the data are handled as a

21-year running mean and running mean values were assigned to the last year of each window period. We calculate anomalies with respect to the mean of the first 21 years of the RCP8.5 scenario (2006–2026). As we are interested in the land processes in the Arctic, most variables are considered only over land. The only exception is global mean temperature (T_{glob}), derived from the surface temperature variable from the atmosphere component output of the model. To calculate the mean over an area, we apply a cosine-weighted mean. The three ensembles are generally considered as a mean for each RFG method individually. If not stated otherwise, the T_{xx} is calculated as the maximum of the mean monthly T_{xx} of the JJA months for each year, minimum temperature (T_{Nn}) as the minimum of the mean monthly minimum temperature of the DJF months for each year (December being taken from the year prior) and mean temperature (T_{mean}) as the mean temperature of all months of the respective year. The monthly T_{xx} , T_{Nn} and T_{mean} were all derived from the respective (daily) maximum, minimum, mean of average 2 m temperature from the land component output by averaging the daily values for each month. We define albedo as upward/downward clear-sky shortwave radiation at the surface. The upward clear-sky shortwave radiation is calculated by subtracting the net from the downward clear-sky shortwave radiation at the surface.

To assess how the Arctic temperature regimes shift under RFG, we analyse the current (2001–2020) observed T_{xx} and T_{mean} JJA conditions for a satellite data-driven burned area dataset (MCD64)⁵⁴. The burned area per T_{xx} and T_{mean} anomaly combination is evaluated by calculating the extent of burned area per T_{xx} and T_{mean} anomaly combination (Fig. 4a). The monthly surface temperature corresponding to the fire activity is quantified using Climatic Research Unit TS4.01⁵⁵. The anomalies are calculated for each grid cell with respect to the average of JJA T_{xx} and T_{mean} from 2001 to 2020 for that grid cell. We further analyse the JJA T_{xx} frequency under RCP4.5 at the end of the century to count frequencies under a given mean and T_{xx} anomalies in the Arctic (Fig. 4b) and how the temperature frequencies shift under CCT and MCB (Fig. 4c, d). To determine anomalies for the NorESM1-ME datasets, average JJA T_{xx} and T_{mean} are calculated for each grid cell for the first 21 years (2006–2026) of RCP4.5 and subtracted from T_{xx} and T_{mean} of that grid cell in 2100 for RCP4.5, CCT and MCB. The permafrost fraction is calculated based on a dataset of the European Space Agency's Climate Change Initiative Permafrost project and covers the period from 2003 to 2019⁵⁸. The monthly surface temperature corresponding to the permafrost fraction is quantified using Climatic Research Unit TS4.01⁵⁵. No anomalies are determined for T_{Nn} as permafrost thawing depends on absolute temperatures and is not anomaly-driven like fires. We determine the temperature frequencies by making 0.6 by $0.6 \text{ }^\circ\text{C}$ (Figs. 4) and 2.0 by $3.0 \text{ }^\circ\text{C}$ (Fig. 6) bins and evaluating how often each T_{xx} or T_{Nn} and T_{mean} (anomaly) combination is present in all the land grid cells north of 50 and 65°N , respectively, divided by the number of total land grid cells north of 50 and 65°N , respectively. To analyse the shift in temperature conditions under CCT and MCB in 2100 the frequencies from RCP4.5 in 2100 are subtracted. Only grid cells that contain at least 50% of Arctic plant function types (needleleaf evergreen boreal tree, needleleaf deciduous boreal tree, broadleaf deciduous boreal tree, broadleaf deciduous boreal shrub and C3 arctic grass) are considered for the fire plots. We calculate the temperature conditions for fires by calculating the total burned area for the respective temperature conditions from the MCD64 monthly burned area dataset from 2001 to 2020 and the same time frame for the temperature anomalies. Similarly, the temperature conditions corresponding to the permafrost fraction are calculated by determining the mean permafrost fraction per respective temperature conditions from 2003 to 2019. As single heat events are important for fires, we consider the JJA months separately for the fire plots, while for the permafrost plots, the DJF months are taken as a mean, since longer cold or warm periods are more influential than shorter events. The permafrost area versus T_{Nn} is calculated from the RCP4.5 data (Supplementary Fig. 11). The area of permafrost is calculated yearly and defined as the summed area of the grid cells where T_{mean} was below $0 \text{ }^\circ\text{C}$ for at least the two previous years. Similarly, the area of permafrost at the end of the century for RCP4.5 and SAI is calculated yearly as the area of the grid cells

where T_{mean} was below 0 °C for at least two consecutive years. Reported is the mean area of the last 21 years of the century (2080–2100).

The shift in the distribution of the difference of daily JJA T_{Xx} anomaly and JJA T_{mean} anomaly for RCP4.5, CCT and MCB is visualised with normalised histograms. The anomalies are calculated for the last 21 years of the simulation as a difference of the daily temperature of each grid cell to the mean temperature of the grid cell during that month from 2006 to 2026. This was done separately for June, July and August.

Statistical analysis

To assess the spatial differences between the RFG and the RCP4.5 scenarios we perform a LR analysis. While many components of the climate system do not behave in a linear way, we chose this method as it is easy to compute, visualise and interpret its coefficients. LR allows for an easy assessment of spatial differences of single variables such as global mean temperature and precipitation. We calculate T_{glob} of each ensemble for the timespan 2006–2100 for RCP4.5 and 2020–2100 for RFG with a cosine-weighted mean and a 21-year running mean. To simplify the description of the methods, the following explanation is given on the example of transpiration under CCT, however, the method can be applied for all used variables (e.g., T_{Xx} , T_{Nin} , latent heat, precipitation) and RFG method (CCT, MCB, SAI) of this study. In the example of Fig. 2a, we calculate the JJA mean of transpiration as a 21-year running mean for every land grid cell for all three CCT ensembles and the RCP4.5 scenario and evaluate its dependence on T_{glob} using LR. We perform a LR for every land grid cell with T_{glob} as independent and the transpiration of that grid cell as dependent variable for every ensemble. The difference in slope plotted in Fig. 2a represents the difference of the mean slope of the three CCT ensembles and the RCP4.5 slope.

To test for significant differences between CCT and RCP4.5 we use the obtained slope and interception values to predict transpiration values of the last 21 years for each grid cell and calculate the residual by subtracting the simulated transpiration value. The residual is calculated twice per CCT ensemble, using the simulated transpiration and T_{glob} of that ensemble: once with the slope and intercept from the LR of that CCT ensemble and once with the slope and intercept from the RCP4.5 LR. The residuals are compared using an unpaired t-test. Assuming there are no differences between CCT and RCP4.5, Eq. (1) should yield the same result for the LR results for both CCT and RCP4.5:

$$b = \text{Transpiration}_{\text{CCT}(n)}[i] - \text{slope}_{\text{RCP or CCT}(n)} \cdot T_{\text{glob,CCT}(n)}[i] - \text{intercept}_{\text{RCP or CCT}(n)}, \quad (1)$$

where $n = 1, 2, 3$, represents the three CCT ensembles, i is for last year of the 21-year running mean and slope and intercept represent the slope and intercept for RCP4.5 and the three CCT ensembles. Hence, when conducting an unpaired t-test for the b values obtained for the slope and intercept of the RCP4.5 LR and the b values obtained for the slopes and intercepts of the CCT LRs, $p < 0.05$ indicate a significant difference between the residuals of the LRs of CCT and RCP4.5.

Data availability

The NorESM1-ME model is described in detail in ref. 13 and ref. 14. The RCP8.5 and RCP4.5 data output from NorESM1-ME is available under <https://doi.org/10.11582/2019.00007> while the CCT, MCB and SAI output is available under <https://doi.org/10.11582/2023.00004>. Source data are provided under <https://doi.org/10.6084/m9.figshare.25244725>.

Code availability

The codes used to generate the results and Figures of this work are available at github repository (<https://github.com/RhondaMueller/Codes-RFG-Arctic-Impacts.git>).

Received: 3 September 2023; Accepted: 18 March 2024;

Published online: 05 April 2024

References

1. UNFCCC. Paris Agreement. *Decision 1CP21* (2015).
2. Roelfsema, M. et al. Taking stock of national climate policies to evaluate implementation of the Paris Agreement. *Nat. Commun.* **11**, 2096 (2020).
3. Riahi, K. et al. Mitigation pathways compatible with long-term goals. In *Proc. IPCC, 2022: Climate Change 2022: Mitigation of Climate Change*. Contribution of Working Group III to the Sixth Assessment Report of the Intergovernmental Panel on Climate Change (Cambridge University Press, 2022).
4. Lawrence, M. G. et al. Evaluating climate geoengineering proposals in the context of the Paris Agreement temperature goals. *Nat. Commun.* **9**, 3734 (2018).
5. Muri, H. et al. Climate response to aerosol geoengineering: a multimethod comparison. *J. Clim.* **31**, 6319–6340 (2018).
6. Russell, L. M. et al. Ecosystem impacts of geoengineering: a review for developing a science plan. *Ambio* **41**, 350–369 (2012).
7. Shepherd, J. K. *Geoengineering the climate: science, governance and uncertainty*. (The Royal Society, 2009).
8. Smith, W. The cost of stratospheric aerosol injection through 2100. *Environ. Res. Lett.* **15**, 114004 (2020).
9. Mitchell, D. L. & Finnegan, W. Modification of cirrus clouds to reduce global warming. *Environ. Res. Lett.* **4**, 045102 (2009).
10. Ahlm, L. et al. Marine cloud brightening—as effective without clouds. *Atmospheric Chem. Phys.* **17**, 13071–13087 (2017).
11. Latham, J. Control of global warming? *Nature* **347**, 339–340 (1990).
12. Kellogg, W. W. & Schneider, S. H. Climate stabilization: for better or for worse? *Science* **186**, 1163–1172 (1974).
13. Bentsen, M. et al. The Norwegian Earth System Model, NorESM1-M—Part 1: description and basic evaluation of the physical climate. *Geosci. Model Dev.* **6**, 687–720 (2013).
14. Tjiputra, J. F. et al. Evaluation of the carbon cycle components in the Norwegian Earth System Model (NorESM). *Geosci. Model Dev.* **6**, 301–325 (2013).
15. Tilmes, S., Sanderson, B. M. & O’Neill, B. C. Climate impacts of geoengineering in a delayed mitigation scenario. *Geophys. Res. Lett.* **43**, 8222–8229 (2016).
16. Jones, A. C., Haywood, J. M. & Jones, A. Climatic impacts of stratospheric geoengineering with sulfate, black carbon and titania injection. *Atmos. Chem. Phys.* **16**, 2843–2862 (2016).
17. Keller, D. P., Feng, E. Y. & Oeschles, A. Potential climate engineering effectiveness and side effects during a high carbon dioxide-emission scenario. *Nat. Commun.* **5**, 3304 (2014).
18. Da-Allada, C. Y. et al. Changes in West African summer monsoon precipitation under stratospheric aerosol geoengineering. *Earths Future* **8**, e2020EF001595 (2020).
19. Fan, Y. et al. Solar geoengineering can alleviate climate change pressures on crop yields. *Nat. Food* **2**, 373–381 (2021).
20. Lauvset, S. K., Tjiputra, J. & Muri, H. Climate engineering and the ocean: effects on biogeochemistry and primary production. *Biogeosciences* **14**, 5675–5691 (2017).
21. Tjiputra, J. F., Grini, A. & Lee, H. Impact of idealized future stratospheric aerosol injection on the large-scale ocean and land carbon cycles. *J. Geophys. Res. Biogeosci.* **121**, 2–27 (2016).
22. Park, C.-E. et al. Inequal responses of drylands to radiative forcing geoengineering methods. *Geophys. Res. Lett.* **46**, 14011–14020 (2019).
23. Berdahl, M. et al. Arctic cryosphere response in the Geoengineering Model Intercomparison Project G3 and G4 scenarios. *J. Geophys. Res. Atmos.* **119**, 1308–1321 (2014).
24. Chen, Y., Liu, A. & Moore, J. C. Mitigation of Arctic permafrost carbon loss through stratospheric aerosol geoengineering. *Nat. Commun.* **11**, 2430 (2020).
25. Lee, W. R. et al. High-latitude stratospheric aerosol injection to preserve the Arctic. *Earths Future* **11**, e2022EF003052 (2023).

26. Lee, H. et al. The response of permafrost and high-latitude ecosystems under large-scale stratospheric aerosol injection and its termination. *Earths Future* **7**, 605–614 (2019).
27. Jones, A., Haywood, J. & Boucher, O. A comparison of the climate impacts of geoengineering by stratospheric SO₂ injection and by brightening of marine stratocumulus cloud. *Atmos. Sci. Lett.* **12**, 176–183 (2011).
28. Yu, X. et al. Impacts, effectiveness and regional inequalities of the GeoMIP G1 to G4 solar radiation management scenarios. *Glob. Planet. Change* **129**, 10–22 (2015).
29. Rantanen, M. et al. The Arctic has warmed nearly four times faster than the globe since 1979. *Commun. Earth Environ.* **3**, 1–10 (2022).
30. Kim, J.-S. et al. Reduced North American terrestrial primary productivity linked to anomalous Arctic warming. *Nat. Geosci.* **10**, 572–576 (2017).
31. Kim, J.-S. et al. Arctic warming-induced cold damage to East Asian terrestrial ecosystems. *Commun. Earth Environ.* **3**, 1–8 (2022).
32. IPCC. *Climate Change 2022: Impacts, Adaptation, and Vulnerability. Contribution of Working Group II to the Sixth Assessment Report of the Intergovernmental Panel on Climate Change.* (eds Pörtner, H.-O. et al.) 3056 (Cambridge University Press, Cambridge, UK and New York, NY, USA, 2022).
33. Drake, B. G., Gonzalez-Meler, M. A. & Long, S. P. More efficient plants: a consequence of rising atmospheric CO₂? *Annu. Rev. Plant Physiol. Plant Mol. Biol.* **48**, 609–639 (1997).
34. Muri, H., Niemeier, U. & Kristjánsson, J. E. Tropical rainforest response to marine sky brightening climate engineering. *Geophys. Res. Lett.* **42**, 2951–2960 (2015).
35. Zhu, Z. et al. Greening of the Earth and its drivers. *Nat. Clim. Change* **6**, 791–795 (2016).
36. Zeng, Z. et al. Climate mitigation from vegetation biophysical feedbacks during the past three decades. *Nat. Clim. Change* **7**, 432–436 (2017).
37. Mansfield, T. A., Hetherington, A. M. & Atkinson, C. J. Some current aspects of stomatal physiology. *Annu. Rev. Plant Physiol. Plant Mol. Biol.* **41**, 55–75 (1990).
38. Park, S.-W., Kim, J.-S. & Kug, J.-S. The intensification of Arctic warming as a result of CO₂ physiological forcing. *Nat. Commun.* **11**, 2098 (2020).
39. Lemordant, L. & Gentine, P. Vegetation response to rising CO₂ impacts extreme temperatures. *Geophys. Res. Lett.* **46**, 1383–1392 (2019).
40. Niemeier, U. & Timmreck, C. What is the limit of climate engineering by stratospheric injection of SO₂? *Atmos. Chem. Phys.* **15**, 9129–9141 (2015).
41. Duffey, A., Irvine, P., Tsamados, M. & Stroeve, J. Solar geoengineering in the polar regions: a review. *Earths Future* **11**, e2023EF003679 (2023).
42. Lee, H., Muri, H., Ekici, A., Tjiputra, J. & Schwinger, J. The response of terrestrial ecosystem carbon cycling under different aerosol-based radiation management geoengineering. *Earth Syst. Dyn.* **12**, 313–326 (2021).
43. Ainsworth, E. A. & Long, S. P. What have we learned from 15 years of free-air CO₂ enrichment (FACE)? A meta-analytic review of the responses of photosynthesis, canopy properties and plant production to rising CO₂. *New Phytol.* **165**, 351–372 (2005).
44. Lammertsma, E. I. et al. Global CO₂ rise leads to reduced maximum stomatal conductance in Florida vegetation. *Proc. Natl. Acad. Sci.* **108**, 4035–4040 (2011).
45. Seneviratne, S. I. et al. Investigating soil moisture–climate interactions in a changing climate: a review. *Earth-Sci. Rev.* **99**, 125–161 (2010).
46. Miralles, D. G., Teuling, A. J., van Heerwaarden, C. C. & Vilà-Guerau de Arellano, J. Mega-heatwave temperatures due to combined soil desiccation and atmospheric heat accumulation. *Nat. Geosci.* **7**, 345–349 (2014).
47. Kala, J. et al. Impact of the representation of stomatal conductance on model projections of heatwave intensity. *Sci. Rep.* **6**, 23418 (2016).
48. Skinner, C. B., Poulsen, C. J. & Mankin, J. S. Amplification of heat extremes by plant CO₂ physiological forcing. *Nat. Commun.* **9**, 1094 (2018).
49. Kristjánsson, J. E., Muri, H. & Schmidt, H. The hydrological cycle response to cirrus cloud thinning. *Geophys. Res. Lett.* **42**, 10,807–10,815 (2015).
50. Kharuk, V. I. et al. Wildfires in the Siberian taiga. *Ambio* **50**, 1953–1974 (2021).
51. Young, A. M., Higuera, P. E., Duffy, P. A. & Hu, F. S. Climatic thresholds shape northern high-latitude fire regimes and imply vulnerability to future climate change. *Ecography* **40**, 606–617 (2017).
52. Bowman, D. M. J. S. et al. Human exposure and sensitivity to globally extreme wildfire events. *Nat. Ecol. Evol.* **1**, 1–6 (2017).
53. Scholten, R. C., Jandt, R., Miller, E. A., Rogers, B. M. & Veraverbeke, S. Overwintering fires in boreal forests. *Nature* **593**, 399–404 (2021).
54. Giglio, L., Justice, C., Boschetti, L. & Roy, D. MCD64A1 MODIS/Terra +Aqua Burned Area Monthly L3 Global 500m SIN Grid V006 [Data set]. NASA EOSDIS Land Process. DAAC, accessed 26 April 2023 from <https://doi.org/10.5067/MODIS/MCD64A1.006>.
55. Harris, I., Jones, P. D., Osborn, T. J. & Lister, D. H. Updated high-resolution grids of monthly climatic observations—the CRU TS3.10 Dataset. *Int. J. Climatol.* **34**, 623–642 (2014).
56. Schuur, E. A. G. et al. Vulnerability of permafrost carbon to climate change: implications for the global carbon cycle. *BioScience* **58**, 701–714 (2008).
57. Schuur, E. A. G. et al. Climate change and the permafrost carbon feedback. *Nature* **520**, 171–179 (2015).
58. Obu, J. et al. ESA Permafrost Climate Change Initiative (Permafrost_cci): Permafrost extent for the Northern Hemisphere, v3.0. NERC EDS Cent. Environ. Data Anal. <https://doi.org/10.5285/6e2091cb0c8b4106921b63cd5357c97c> (2021).
59. Curry, C. L. et al. A multimodel examination of climate extremes in an idealized geoengineering experiment. *J. Geophys. Res. Atmos.* **119**, 3900–3923 (2014).
60. Bednarz, E. M. et al. Injection strategy—a driver of atmospheric circulation and ozone response to stratospheric aerosol geoengineering. *Atmos. Chem. Phys.* **23**, 13665–13684 (2023).
61. Tully, C., Neubauer, D., Omanovic, N. & Lohmann, U. Cirrus cloud thinning using a more physically based ice microphysics scheme in the ECHAM-HAM general circulation model. *Atmos. Chem. Phys.* **22**, 11455–11484 (2022).
62. McCarty, J. L., Smith, T. E. L. & Turetsky, M. R. Arctic fires re-emerging. *Nat. Geosci.* **13**, 658–660 (2020).
63. Tokarska, K. B. et al. Past warming trend constrains future warming in CMIP6 models. *Sci. Adv.* **6**, eaaz9549 (2020).
64. Plazzotta, M., Séférian, R., Douville, H., Kravitz, B. & Tjiputra, J. Land surface cooling induced by sulfate geoengineering constrained by major volcanic eruptions. *Geophys. Res. Lett.* **45**, 5663–5671 (2018).
65. Chylek, P., Folland, C., Klett, J. D. & Dubey, M. K. CMIP5 climate models overestimate cooling by volcanic aerosols. *Geophys. Res. Lett.* **47**, e2020GL087047 (2020).
66. Iversen, T. et al. The Norwegian earth system model, NorESM1-M—Part 2: climate response and scenario projections. *Geosci. Model Dev.* **6**, 389–415 (2013).
67. Liu, W., Fedorov, A. V., Xie, S.-P. & Hu, S. Climate impacts of a weakened Atlantic Meridional Overturning Circulation in a warming climate. *Sci. Adv.* **6**, eaaz4876 (2020).

68. Kravitz, B. et al. The geoengineering model intercomparison project phase 6 (GeoMIP6): simulation design and preliminary results. *Geosci. Model Dev.* **8**, 3379–3392 (2015).
69. Taylor, K. E., Stouffer, R. J. & Meehl, G. A. An overview of CMIP5 and the experiment design. *Bull. Am. Meteorol. Soc.* **93**, 485–498 (2012).
70. Crook, J. A., Jackson, L. S., Osprey, S. M. & Forster, P. M. A comparison of temperature and precipitation responses to different Earth radiation management geoengineering schemes. *J. Geophys. Res. Atmos.* **120**, 9352–9373 (2015).
71. Taylor, P. C. et al. Process drivers, inter-model spread, and the path forward: a review of amplified Arctic warming. *Front. Earth Sci.* **9**, 758361 (2022).
72. Deng, J., Dai, A. & Xu, H. Nonlinear climate responses to increasing CO₂ and anthropogenic aerosols simulated by CESM1. *J. Clim.* **33**, 281–301 (2020).
73. Tilmes, S. et al. CESM1(WACCM) stratospheric aerosol geoengineering large ensemble project. *Bull. Am. Meteorol. Soc.* **99**, 2361–2371 (2018).
74. Kirkevåg, A. et al. Aerosol–climate interactions in the Norwegian Earth System Model—NorESM1-M. *Geosci. Model Dev.* **6**, 207–244 (2013).
75. Oleson, K. W. et al. Technical Description of version 4.0 of the Community Land Model (CLM). <https://doi.org/10.5065/D6FB50WZ> (2010).
76. Lawrence, D. M. et al. Parameterization improvements and functional and structural advances in Version 4 of the Community Land Model. *J. Adv. Model. Earth Syst.* **3**, 03001 (2011).
77. Hurr, G. C. et al. The underpinnings of land-use history: three centuries of global gridded land-use transitions, wood-harvest activity, and resulting secondary lands. *Glob. Change Biol.* **12**, 1208–1229 (2006).
78. Lawrence, P. J. et al. Simulating the biogeochemical and biogeophysical impacts of transient land cover change and wood harvest in the Community Climate System Model (CCSM4) from 1850 to 2100. *J. Clim.* **25**, 3071–3095 (2012).
79. Muri, H., Kristjánsson, J. E., Storelvmo, T. & Pfeffer, M. A. The climatic effects of modifying cirrus clouds in a climate engineering framework. *J. Geophys. Res. Atmospheres* **119**, 4174–4191 (2014).
80. Latham, J. Amelioration of global warming by controlled enhancement of the albedo and longevity of low-level maritime clouds. *Atmos. Sci. Lett.* **3**, 52–58 (2002).
81. Mårtensson, E. M., Nilsson, E. D., de Leeuw, G., Cohen, L. H. & Hansson, H.-C. Laboratory simulations and parameterization of the primary marine aerosol production. *J. Geophys. Res. Atmospheres* **108**, 4297 (2003).
82. Alterskjær, K. & Kristjánsson, J. E. The sign of the radiative forcing from marine cloud brightening depends on both particle size and injection amount. *Geophys. Res. Lett.* **40**, 210–215 (2013).
83. Crutzen, P. J. Albedo enhancement by stratospheric sulfur injections: a contribution to resolve a policy dilemma? *Clim. Change* **77**, 211–220 (2006).
84. Tilmes, S. et al. A new Geoengineering Model Intercomparison Project (GeoMIP) experiment designed for climate and chemistry models. *Geosci. Model Dev.* **8**, 43–49 (2015).
85. Niemeier, U. et al. Initial fate of fine ash and sulfur from large volcanic eruptions. *Atmos. Chem. Phys.* **9**, 9043–9057 (2009).

Acknowledgements

The NorESM1-ME simulations were performed on resources provided by Sigma2—the National Infrastructure for High Performance Computing and Data Storage in Norway accounts nn9182k, nn9448k, NS2345K and NS9033K. J.-S. K. was supported by the Center for Ocean Research in Hong Kong and Macau (CORE), which is a joint ocean research center for ocean research between Laoshan Laboratory and the Hong Kong University of Science and Technology.

Author contributions

R.C. M. conducted analyses, prepared Figures and wrote the manuscript. R.C. M. and J.-S. K. designed the research and wrote the majority of the manuscript content. H. M. and J. T. performed model simulations. H. M., H. L. and J. T. provided the output of the NorESM1-ME simulations. R.C. M., J.-S. K., H. M., H. L., J. T., J.-H. Y. and G. S.-S. discussed the results and revised the manuscript.

Competing interests

The authors declare no competing interests.

Additional information

Supplementary information The online version contains supplementary material available at <https://doi.org/10.1038/s43247-024-01329-3>.

Correspondence and requests for materials should be addressed to Rhonda C. Müller or Jin-Soo Kim.

Peer review information *Communications Earth & Environment* thanks Hera Gudlaugsdottir and the other, anonymous, reviewer(s) for their contribution to the peer review of this work. Primary Handling Editors: Min-Hui Lo and Aliénor Lavergne. A peer review file is available.

Reprints and permissions information is available at <http://www.nature.com/reprints>

Publisher's note Springer Nature remains neutral with regard to jurisdictional claims in published maps and institutional affiliations.

Open Access This article is licensed under a Creative Commons Attribution 4.0 International License, which permits use, sharing, adaptation, distribution and reproduction in any medium or format, as long as you give appropriate credit to the original author(s) and the source, provide a link to the Creative Commons licence, and indicate if changes were made. The images or other third party material in this article are included in the article's Creative Commons licence, unless indicated otherwise in a credit line to the material. If material is not included in the article's Creative Commons licence and your intended use is not permitted by statutory regulation or exceeds the permitted use, you will need to obtain permission directly from the copyright holder. To view a copy of this licence, visit <http://creativecommons.org/licenses/by/4.0/>.

© The Author(s) 2024